

Tracking cold water upwelling filaments in the ocean using matched-field inversion

V. Corré, S. Jesus

SiPLAB-FCT, Universidade do Algarve, PT-8000 Faro, Portugal.

Summary

A new application of a matched-field inversion method for estimating the range and time variability of ocean properties is presented. The method uses acoustic data from a single array-source pair. Since estimating range-dependent properties with such a simple configuration is a problem whose solution is not unique, the primary objective is to obtain the variability trend rather than very accurate estimates of the properties. The inversion method is applied to a synthetic data set obtained during the simulated development of an upwelling filament. The objective consists in estimating the sound-speed profile of the filament, its position and width, and the variations of these properties with time. The performance of the method is first tested in the ideal case where no noise nor model mismatch is present. Results show the feasibility of tracking the upwelling and obtaining good accuracy for the parameter estimates within a reasonable computational time. The presence of noise in the data or model mismatch degrades the accuracy of the parameter estimates. However the global rise of cold water can still be detected and localized under realistic conditions. Although the filament properties as well as the source and array positions have noticeable effects on the inversion results, no clear evidence of a parameter hierarchy was found.

PACS no. XXX.Ra, XXX.Qi

1. Introduction

ATOMS¹ is a project that aims at developing a monitoring system of the ocean variability using acoustic tomography. A preliminary test for this system is to monitor the recurrent upwelling filament that develops off Cape São Vicente (Portugal) [1, 2], using a single vertical array of receivers and a towed source. This paper presents a synthetic study that simulates the monitoring conditions of this particular region and intends to check the feasibility and limits of such a monitoring.

The estimation of range-dependent properties with a single array-source pair is a problem whose solution is not unique. Being aware that this difficulty is particularly true when data are contaminated with noise (i.e., in all real cases), the objective was to obtain a variability trend rather than very accurate estimates of the properties. In other words, detection and global tracking of the filaments were of prime interest rather than detailed mapping of the sea-temperature (or sound-speed) field.

While acoustic travel-time tomography [3] is now a well-developed technique for large-scale, deep-ocean regions, it is less adapted for studying filaments which are mesoscale features that develop in relatively shallow areas. Using matched-field processing to estimate ocean sound speed [4, 5, 6] is a more recent approach than tomography. However this approach has already shown good results and can treat any type of environment equally. It is therefore the approach adopted in this study.

This paper is organised as follows. A brief description of upwelling filaments is given in Section 2. The waveguide model chosen to represent the range-dependent environment and the model parameters are defined in Section 3. Section 4 describes the matched-field inversion (MFI) method used to estimate the model parameters. Inversion results obtained for simulated data in ideal and non-ideal (i.e., more realistic) cases are shown in Section 5. Finally, some conclusions are given in Section 6.

2. Upwelling filaments

Eastern ocean boundaries are regions of high upwelling occurrence. The upwellings of the California current system (CCS) and of the Atlantic coast of the Iberian peninsula have received particular attention [1-2,7-11]. Together with high-accuracy satellite images, these studies show not only a coastal band of upwelled water but also mesoscale features such as eddies, meanders and cold filaments developing from the band and pointing offshore. Due to their major role in the mass exchange between coastal and offshore waters, filaments represent important ocean entities to study and understand.

Most of the knowledge about the formation of the upwelling filaments [7], their spatial structure [8, 9] (see Figure 1) and their mass transport [9] is derived from measurements done during the Coastal Transition Zone Program [10] in the CCS. However strong similarities exist between the basic circulation patterns of the CCS and the Iberian peninsula [11]; and a few authors [1, 2] have investigated the basic features of the upwelling filaments off the Iberian peninsula. According to the studies specific to this region, the upwelling season starts in May-June. At that stage, cold fingers of water (15-30 km in length) develop

Received 1 January 1993,
accepted 1 January 1993.

¹ Acoustic TOMography Monitoring System

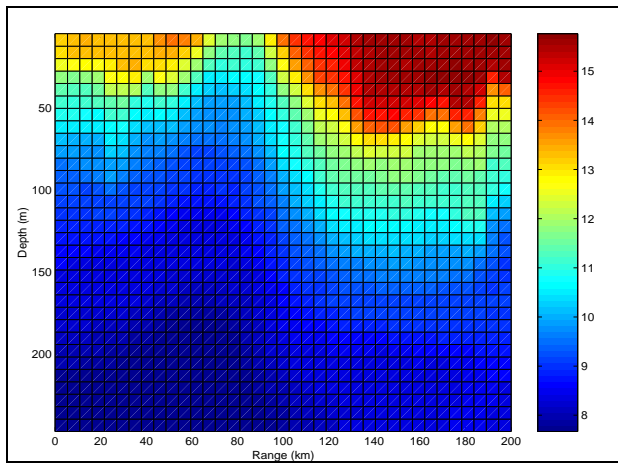


Figure 1. Spatial variations of the temperature in a region featuring an upwelling filament (from [8]).

off the upwelling. Some of the cold fingers then grow into filaments that reach, at the end of August, a maximum length and width of 250 km and 50 km respectively. Finally, the filaments disappear after the upwelling season. At the surface, the difference of temperature between filaments and surrounding waters is about 2 to 3°C. The distance between filaments varies between 80 to 150 km and their locations appear to be connected to the presence of capes and submarine ridges. The filament developing at Cape São Vicente, a discontinuity in the eastern boundary, represents therefore a particular region of interest.

3. Parameterization of the environment

The parameterization of the ocean environment is a delicate issue since the inversion results depend on the environment model adopted while the form of the real ocean waveguide is usually unknown. An inappropriate model can be a source of mismatch, a situation where the minimum misfit does not correspond to the true ocean properties, and can lead to poor estimates. Usually, independent *a priori* information guides the choice of the model. When modeling a range-dependent environment, the choice of the model also depends on the desired accuracy of the estimates. In the present case, since the primary interest was detecting mesoscale ocean features rather than obtaining a detailed mapping, a coarse model was used to represent the ocean.

Based on the assumption that the source-array vertical plane crosses the filament under study along its width, the water layer in our model (see Figure 2) is gridded into three vertical cells (C_1 , C_2 and C_3) of variable size representing the filament surrounded by “normal” water. Each cell has an independent sound-speed profile. Obviously, this representation would not be a pertinent choice to model an environment which properties vary smoothly and continuously with range. However to detect sharp fronts, such a model is as a good first approximation. In addition, the use of vertical range limits for the middle cell

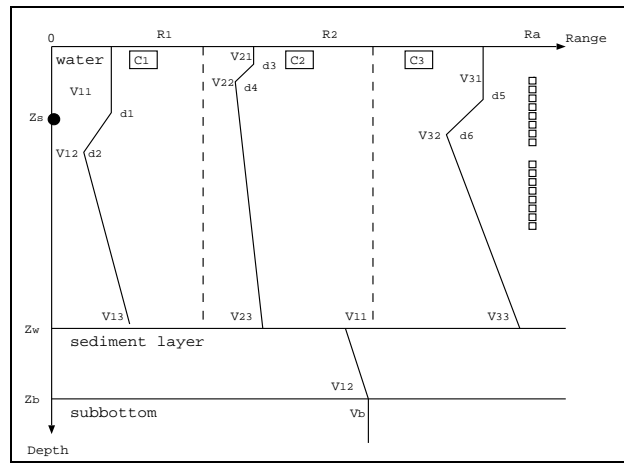


Figure 2. Model of the ocean waveguide. The acoustic source is located at range 0, the vertical line of receivers at range R_a .

is a simplification that is not unrealistic when modeling an upwelling since the water movement is mainly upwards. The rest of the model consists of a sediment layer over a semi-infinite substrate. Each layer (or cell) is characterized by its density, thickness, P- and S-wave velocities and attenuations.

For tomography purposes, the traditional approach to model the sound speed in the water is to use empirical orthogonal functions (EOFs) [4, 5]. This method has been increasingly used since it can provide a high accuracy despite a few coefficients/parameters. On the other hand, a major constraint in using EOFs is that one already needs a good knowledge (through direct measurements or accurate archival data) of the ocean properties to be able to calculate representative eigenfunctions. In the case of monitoring the evolution of a filament for example, the eigenfunctions used should accurately characterize both range and time variability of the sound speed. Therefore, the data samples used to calculate these eigenfunctions should contain the information about this variability. In other words, one would need a relatively large amount of direct measurements in range and time. However, the basic idea behind tomography, or any other remote-sensing method, is precisely to replace direct measurements. Using EOF for acoustic monitoring is therefore contradictory, and instead, we chose to estimate sound-speed points rather than EOF coefficients.

In general, many points are necessary to get a good accuracy of the sound speed. On the other hand, estimating a large number of sound-speed points is an heavy task for an optimization method such as MFI. Once again, considering that the objective was primarily detection rather than accurate mapping of temperature anomalies, a coarse representation of the sound speed that involved few but relevant parameters to estimate was selected. In this representation, the sound-speed profiles are defined with only three points: the sound speed in the homogeneous sea-surface layer, at the lower limit of the thermocline and at the seafloor. Between the depth points, the inverse of the sound-speed squared varies linearly with depth.

There are seven parameters to estimate: three sound speeds of the middle-cell profile (the sound speeds in the two other cells are supposed to be known), the upper and lower limits of the thermocline ($d3$ and $d4$), in order to have a realistic and flexible model, and the range limits of the middle cell (R_1 and R_2), that define the horizontal extent of the filament.

4. Matched-field inversion

In MFI, the estimation of model parameters consists in determining the optimum set of parameters that minimizes the misfit between the measured pressure field and the modeled field calculated for specific parameter values. This section briefly describes the different components of the MFI: the acoustic propagation code that calculates the modeled pressure fields, the cost function that quantifies the misfit, and the search algorithm that samples the parameter space in order to minimize the misfit.

4.1. Propagation code

In order to have a good compromise between accuracy and computational time, all pressure fields (simulated data and replica) were calculated using the SACLANTCEN coupled-mode code C-SNAP [12]. C-SNAP divides a range-dependent environment into several range-independent sections and can therefore handle waveguide models such as the one shown in Figure 2.

4.2. Objective function

To quantify the misfit between the data and replica fields, the frequency-incoherent Bartlett processor was used. The processor can be described as follows. Let $\hat{D}(f)$ represent the normalized data pressure field measured at frequency f , and $\hat{P}^*(\mathbf{m}, f)$ represent the normalized replica field calculated for the model of parameters \mathbf{m} . When the fields have N_f frequency components, the cost function to minimize is given by:

$$E(\mathbf{m}) = 1 - \frac{1}{N_f} \sum_{k=1}^{N_f} |\hat{P}^*(\mathbf{m}, f_k) \hat{D}(f_k)|^2. \quad (1)$$

4.3. Search algorithm

Due to the size of the parameter space and the non-linearity of the problem, neither an exhaustive nor a local search (gradient-type search) were a suitable approach to sample the parameter space. Instead an hybrid algorithm, the simplex genetic algorithm (SGA), was used. This algorithm combines the downhill simplex (DHS) [13] and genetic algorithm (GA) [14] for the local and global search respectively; and has shown good performances in previous inversions [15, 16].

Table I. Time and range-independent parameters.

Parameter	True value
Geometric	
Range of the array R_a (km)	33.5
Shallowest receiver of section 1 (m)	50
Shallowest receiver of section 2 (m)	146
Distance between receivers (m)	4
Source depth Z_s (m)	90
Water depth Z_w (m)	400
Sediment layer	
P-wave velocity at top V_{l1} (m/s)	1600
P-wave velocity at bottom V_{l2} (m/s)	1620
Density ρ_l (g/cm ³)	1.4
S-wave velocity V_{ls} (m/s)	0
P-wave attenuation α_{ls} (dB/ λ)	0.1
S-wave attenuation β_{ls} (dB/ λ)	0
Lower interface depth Z_b (m)	420
Subbottom	
P-wave velocity V_b (m/s)	1800
Density ρ_s (g/cm ³)	2
S-wave velocity V_{bs} (m/s)	0
P-wave attenuation α_{bs} (dB/ λ)	0.5
S-wave attenuation β_{bs} (dB/ λ)	0

5. Simulated study

In order to test the inversion method, it was first applied to synthetic data in the ideal case where there was no source of mismatch. It was then applied to more realistic cases when noise was added to the data and when the waveguide models used to calculate the data and replica were different.

5.1. Ideal case

5.1.1. Synthetic data

The baseline environmental model used to generate synthetic data sets is illustrated in Figure 2. The vertical array was made of two sections of eight receivers. The values of the time and range-independent parameters of the waveguide are given in Table I. Since the computational time increases linearly with the number of frequencies, the pressure fields were calculated only at 250 and 500 Hz. These frequencies are high enough for mode coupling to exist [5] and therefore to make the pressure field measured at the array sensitive to the location of the range-dependent feature of the waveguide [17].

Synthetic time and range-dependent sound-speed profiles were derived from temperatures and salinities measured in an area featuring an upwelling filament [8]. A total of 11 time windows were selected to represent the development of a filament. In the first time window, the sound-speed profiles were identical in all three cells (range-independent ocean). The time variations of the middle-cell profile are illustrated in Figure 3. The profiles in the two other cells did not vary with time and were known during the inversion. (In practice, sound-speed profiles in cells C_1 and C_3 can be estimated by measuring the salinity and temperature profiles at the source and array locations.) The width of the middle cell randomly varied in time within the [11.95 - 12.05 km] interval while the

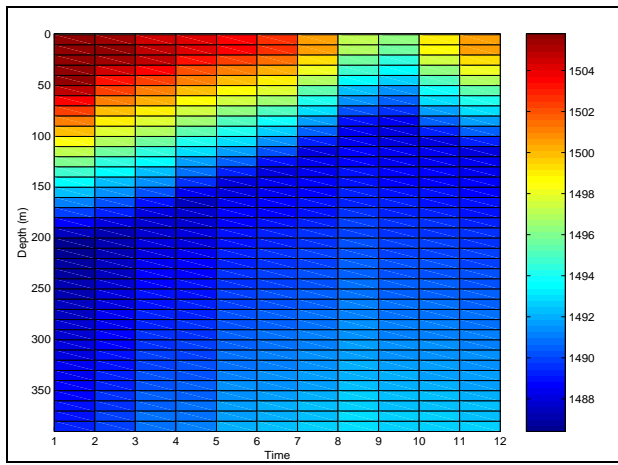


Figure 3. Time variations of the sound-speed profiles in the middle cell. These profiles define the true environment and were derived from the range variations of the temperature and salinity profiles observed in [8].

Table II. Search intervals for the unknown parameters.

Parameter	Search interval
Sound-speed in water (m/s)	1480-1510
Upper limit of the thermocline $d3$ (m)	2-50
Lower limit of the thermocline $d4$ (m)	65-210
Range limit R_1 (km)	10-12
Range limit R_2 (km)	23-24

horizontal distance between the source and the middle-cell front (R_1) varied between 10.95 and 11.05 km. With such a geometry, the middle cell was centered between the source and the array, and its width slightly larger than C_1 or C_3 .

5.1.2. Inversions

The inversion method was applied three times to the data of each time window. Approximately 10000 sets of parameters were tested in each inversion with an initial population of 35 random sets. All known parameters of the waveguide were set to their true value (see Table I) such that, in theory, a global minimum misfit of zero could be reached during the inversion. The search intervals were identical in all inversions and are given in Table II. In practice, the sound speed in the layer surface and at the bottom were defined by positive perturbations of the sound speed at the lower part of the thermocline:

$$V_{21} = V_{22} + v_1; V_{23} = V_{22} + v_2; \quad (2)$$

and v_1 and v_2 were the parameters to estimate rather than V_{21} and V_{23} . The purpose of this change of variables was to introduce some physics in the MFI and to decrease the parameter space. For real data inversions, the choice of the intervals for the range limits R_1 and R_2 would require *a priori* information such as satellite images of sea-surface temperature.

The set of parameters corresponding to the minimum misfit encountered during the three inversions carried out

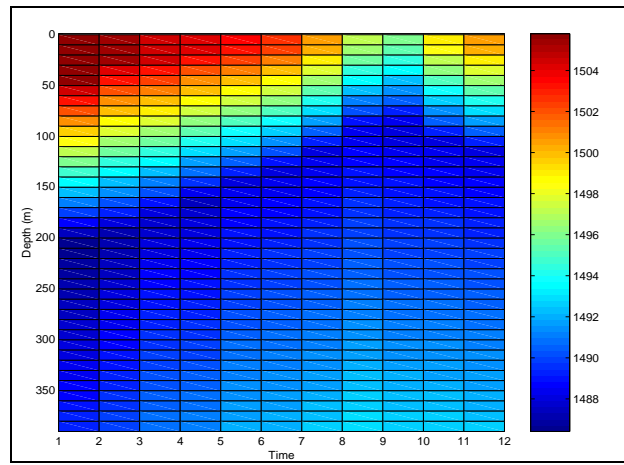


Figure 4. Estimated sound-speed profiles in the middle cell.

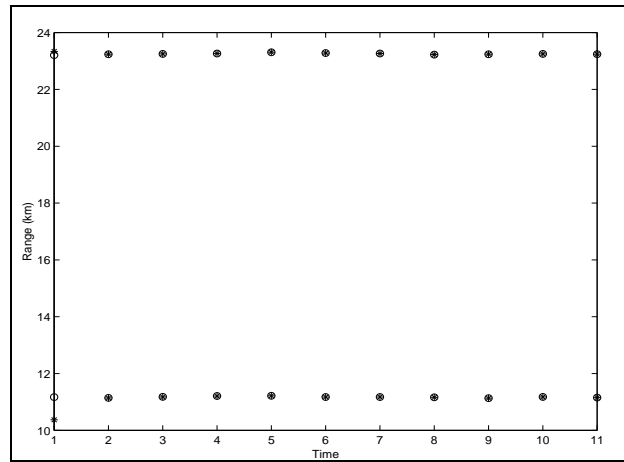


Figure 5. True (circle) and estimated (star) range limits of the middle cell.

for each time window was considered as the parameter estimates. Estimates of the sound-speed profiles and of the range limits of the middle cell are given in Figures 4 and 5 respectively.

The cold-water rising is clearly visible and the range limits are well estimated. Since the environment is range independent in the first time window, the range limits are meaningless for this particular window, and so are their estimates (outliers in Figure 5). Temperatures were deduced from the estimated sound-speed profiles using the sound-speed equation given in [18]. In that case, the maximum and average absolute error (over depth and time) were less than 0.16 and 0.02°C respectively. (The absolute temperatures in the profiles range between 7.5 and 13°C.)

These results show that, for this particular configuration, it is possible to, not only detect the cold water upwelling, but also to obtain an accurate mapping of the sound-speed/temperature profile. However, regarding the temperature estimate, one has to take into account that the temperature profiles were deduced from the estimated sound-speed profiles and the exact salinity profiles. In practice, an error of 1‰ in salinity (i.e., approximately

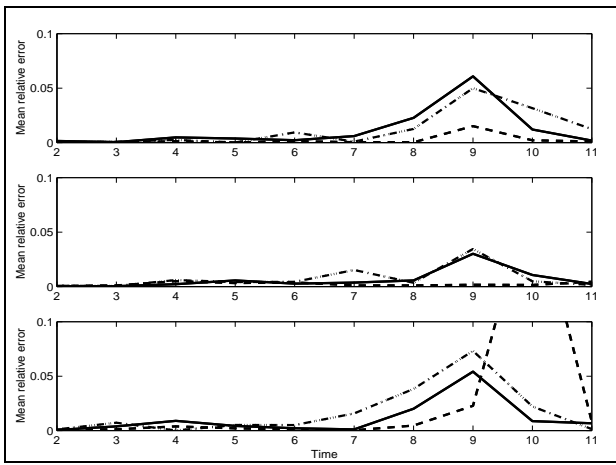


Figure 6. Variations of the parameter mean relative error (ε) with the middle cell location (top: $R_1=5$ km, middle: $R_1=11$ km, bottom: $R_1=17$ km) and width (solid: 12 km, dash: 7 km, dash-dot: 2 km).

the difference introduced by the filament) would lead to a temperature error of 0.4°C . Therefore temperature estimates must be handled carefully.

It is worth noting that the misfits corresponding to these estimates were small (between 10^{-6} and 10^{-4}) but were not the global minimum, i.e., the machine accuracy 10^{-16} . Considering that 1) the parameter accuracy was already relatively good for misfits between 10^{-6} and 10^{-4} , 2) misfits smaller than 10^{-4} were unexpected in realistic scenarios, and 3) global detection was desired rather than accuracy, the number of iterations was fixed to 10000 in the rest of the study. Each inversion took 45 minutes on a Pentium 3 1266 MHz machine.

5.1.3. Effect of middle-cell size and location on the inversion results

When the mode coupling is not negligible, the sensitivity of the pressure field to the sound-speed/temperature anomaly, and therefore the performance of the inversion method, vary with the properties of the anomaly: dimension, location and sound-speed itself. To illustrate the effect of these properties, series of inversions were repeated for three sizes of the middle cell (12, 7 and 2 km) and three locations ($R_1=5$, 11 and 17 km from the source). From one inversion to another, all other parameters were identical, including the inversion parameters (number of iterations, size of GA population etc...). For each inversion, the parameter mean relative error ε was calculated according to Eq. 3:

$$\varepsilon = \frac{1}{N_p} \sum_{p=1}^{N_p} \frac{|m(p) - m_t(p)|}{m_t(p)}, \quad (3)$$

where N_p is the number of parameters ($N_p=7$ here), $m(p)$ is the estimate of the p^{th} parameter and $m_t(p)$ is its true value. The variations of the error with time for all cases are given in Figure 6.

The general observation is that the parameter estimates degrade for the time windows 8, 9 and 10 which correspond to the cases where the homogenous sea-surface layer is very thin (<8 m). For these windows, errors in V_{12} and d_3 , i.e., the parameters associated with the upper layer, have a major contribution in the value of ε . Then, the results show that for identical inversion conditions the best performance of the inversion method is obtained when the middle cell is centered between the source and the array. The effect of the cell width depends on the position of the cell itself. For the 5 and 17 km cell ranges, the 2 and 12 km cell widths provided similar results. However, for most cases, it was possible to obtain a very good approximation of the filament evolution (not shown here).

5.2. Non-ideal cases

In reality, ideal cases such as the one treated above do not occur. Therefore, it is important to know the limitations of the inversion method for more realistic conditions. Here two potential sources of mismatch were investigated: the presence of noise in the data and an erroneous parameterization of the waveguide. These situations imply a non-null global minimum misfit and the fact that this global minimum may not correspond to the true parameters. Since MFI works as a “black box” where the inversion is only driven by minimizing the misfit function, a case-by-case study is necessary to know the effect of a particular mismatch on the parameter estimates.

5.2.1. Effect of correlated noise on the inversion results

Correlated noise $\mathbf{N}(f)$ was added to the original synthetic pressure field $\mathbf{P}(\mathbf{m}, f)$ to generate a new data set $\mathbf{P}'(\mathbf{m}, f)$ according to:

$$\mathbf{P}'(\mathbf{m}, f) = \mathbf{P}(\mathbf{m}, f) + K \cdot \mathbf{N}(f), \quad (4)$$

where K is a vector of real numbers that allows to set the level of noise at each hydrophone h to a given value (see Eq. 7). The noise itself was a sum of two components:

$$N_h(f) = \alpha(f) + \beta_h(f), \quad (5)$$

where $\alpha(f)$ and $\beta_h(f)$ were complex, zero-mean, Gaussian-distributed random numbers. The fact that for a given frequency, the pressure fields at all hydrophones contained an identical component (α) increased the degree of correlation between the pressure fields. On the other hand, β simulated the white-noise component (ambient noise) of the measured pressure fields. Let σ_α and σ_β be the standard deviations of α and β . The noise correlation between hydrophones h and j is given by:

$$\begin{aligned} C_{hj}(f) &= E[N_h(f)N_j^*(f)] \\ &= E[(\alpha(f) + \beta_h(f))(\alpha(f) + \beta_j(f))^*] \\ &= E[(\alpha(f)\alpha^*(f))] + E[\beta_h(f)\beta_j^*(f)] \\ &\quad + E[\beta_h(f)\alpha^*(f)] + E[\alpha(f)\beta_j^*(f)] \end{aligned} \quad (6)$$

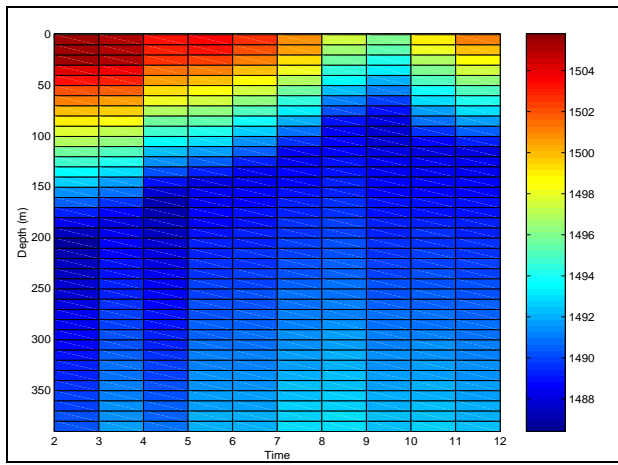


Figure 7. Estimated sound-speed profiles in the middle cell for SNR=10 dB. The true profiles are given in Figure 3.

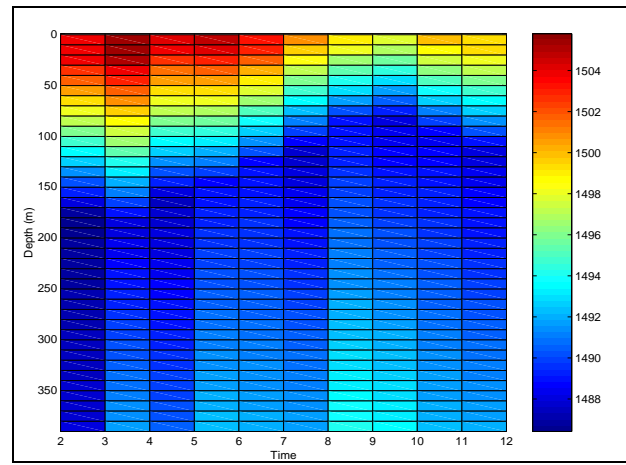


Figure 8. Estimated sound-speed profiles in the middle cell for SNR=5 dB.

Since α and β are independent noise realizations, the last two terms are null and the correlation is reduced to $C_{hj}(f) = \sigma_\alpha$ for $j \neq h$, and $C_{hh}(f) = \sigma_\alpha + \sigma_\beta$ for $j = h$. In practice, σ_α and σ_β were set equal.

The performance of the inversion method was tested for two levels of noise: 10 and 5 dB, the signal-to-noise ratio (SNR) at the h^{th} hydrophone being defined by:

$$\text{SNR}_h = 10 \times \log_{10} \left(\frac{\sum_{i=1}^{N_f} |P'_h(\mathbf{m}, f_i)|^2}{\sum_{i=1}^{N_f} |N_h(f_i)|^2} \right). \quad (7)$$

Inversions were carried out for a middle cell located 11 km from the source and with a width of 12 km. Except for the presence of the noise, the conditions of inversion were the same than for the ideal case. For a given SNR and time window, five different noisy data sets were inverted.

Estimates of the sound-speed profiles obtained with the smallest misfit out of these five inversions are shown in Figures 7 and 8. The error on the range limit estimates (Figure 9) decreases as the degree of range dependence increases. However, despite the presence of noise, the parameter estimates are relatively good and the evolution of the cold filament can still be well observed. In terms of sea-temperature profiles, the mean absolute error over depth and time is 0.056 and 0.126°C for 10 and 5 dB respectively.

Since the global minimum is not known in the presence of noise, it is impossible to know if the inversion algorithm has reached it or not. One can only verify that the minimum misfit encountered is smaller than the misfit calculated for some particular parameter sets. Here, one obvious set to check is the set of true parameters, i.e., the parameters used to generate the noise-free pressure fields. As shown in Figure 10, the misfit calculated with the true parameters is not null and is larger than the minimum misfit encountered for each time window. Standing by itself, this result only stresses the ability of the inversion algorithm to reach regions of low misfit. However the sensitivity curves obtained for the ideal and 5 dB cases (see Figure 11) provide additional insight in the problem as the

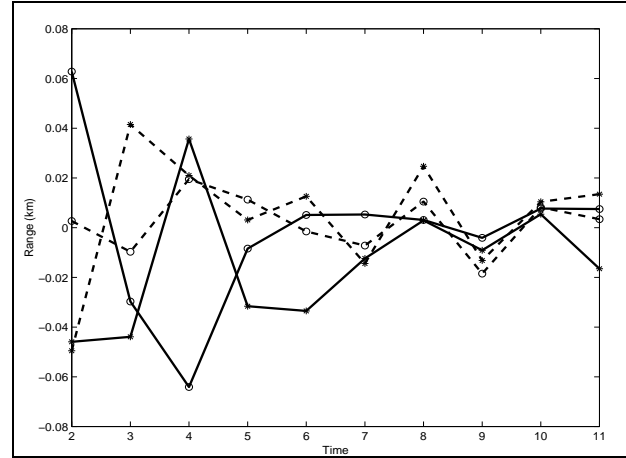


Figure 9. Difference between true and estimated range limits for SNR=10 (circle) and 5dB (star). The solid lines corresponds to R_1 , the dashed lines to R_2 .

two series of curves have very similar behavior and exhibit their global minimum at the parameter true values. Although the generalization to the entire parameter space (multi-dimensional space) is not feasible here, this result can explain the relative robustness of the parameter estimates to the presence of noise in the data.

5.2.2. Effect of model mismatch on the inversion results

In the above, the waveguide models used to calculate the simulated data and replica fields had the same geometry (three layers, three cells, flat bottom etc...). Here the goal is to increase the complexity of the water layer in the true waveguide, while keeping the original parameterization of the replica waveguide in order to test the inversion method in a more realistic scenario. Among the possible approaches to make the waveguide more complex, we chose to introduce transition cells on each side of the middle cell. The parameters of these cells were set to average values between the middle cell and C_1 or C_3 's parameters. The width of the transition cells varied between

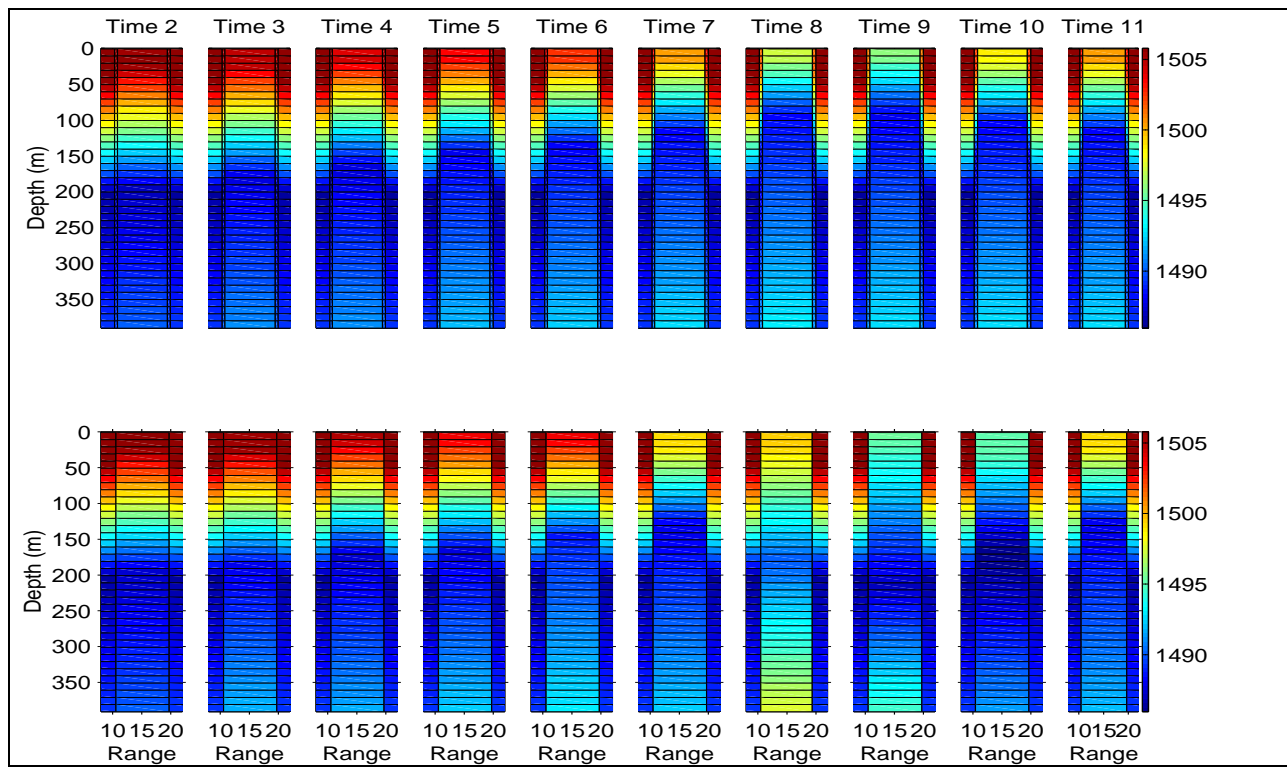


Figure 12. Time variations of the true (top) and estimated (bottom) sound-speed profiles. Transition cells are 500 m wide. Note that for clarity and emphasis on the middle cell properties, only part of cells 1 and 3 (C_1 , C_3) is represented in each panel.

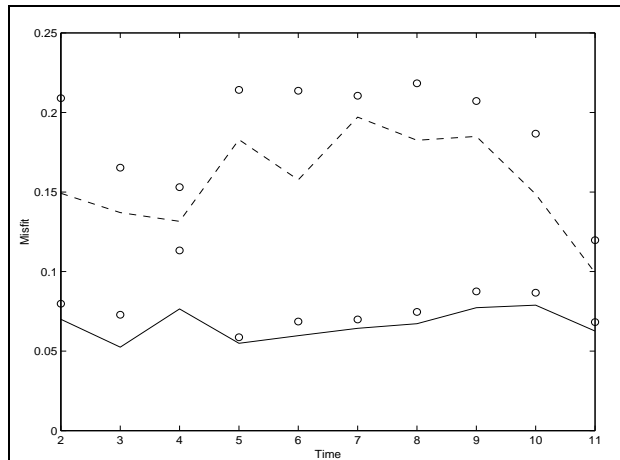


Figure 10. Minimum misfit obtained during the inversions for SNR=10 (solid line) and 5 dB (dashed line). The circles indicate the misfit calculated with the true parameters.

250 and 750 m. The transition cells were overlapping the middle cell in the sense that C_1 and C_3 always had a constant width of 10 and 13 km respectively. The search intervals for the range limits were increased to 3 km wide to include the transition cells. Not surprisingly, it was found that the wider the transition cells, the larger the error in the middle-cell profile estimate. However, up to 500 m wide, the global picture of the cold water upwelling is well visible (Figure 12). Here again, the error is larger for the time windows 8, 9 and 10.

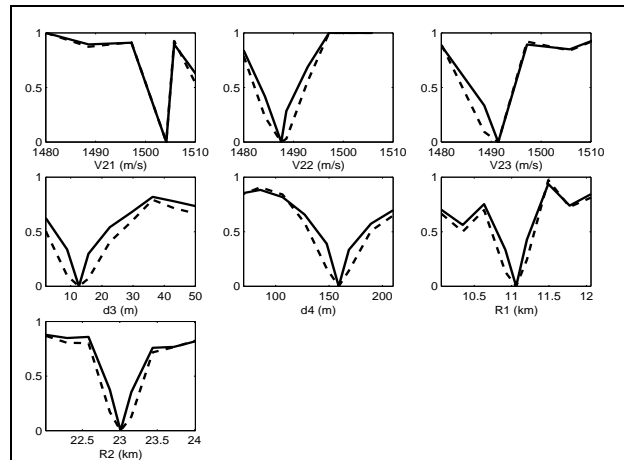


Figure 11. Variations of the misfit with individual parameter, the remaining parameters being fixed to their true value for time window 4, cell width 12 km and distance from source 11 km. The dash line indicates the noise-free case. The solid line shows the average misfit obtained for 15 realizations of correlated noise with SNR=5dB.

As for the noise case, the global minimum is unknown in all scenarios. However here, it is not possible to use the true parameters to verify the algorithm convergence to a low misfit region since the replica waveguide is defined by less parameters than the true waveguide. Nevertheless, for comparison purpose, a reference misfit was calculated with the true parameters of the middle cell. As shown in Figure 13, this reference is relatively large and always larger than the minimum misfit encountered during the se-

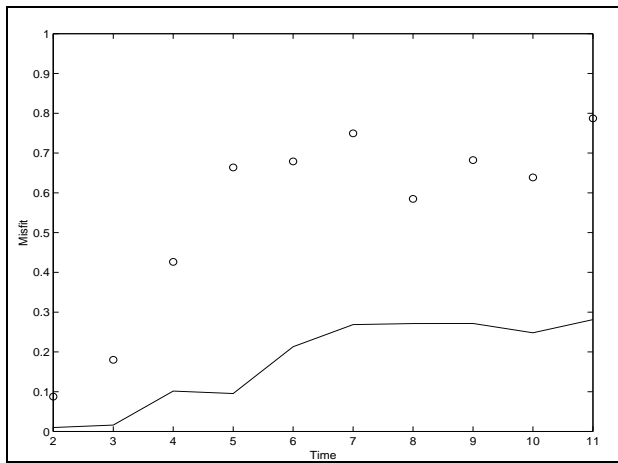


Figure 13. Minimum misfit obtained during the inversions with model mismatch. The circles indicate the misfit calculated with the true parameters of the middle cell. The width of the transition cells was 500 m.

Table III. Location of the source and hydrophones for the different inversion scenarios. The array is defined by the depth of the shallowest hydrophone in each of the two array sections.

Scenario	Array (m)	Z_s (m)
1	50, 146	90
2	114, 146	90
3	50, 82	90
4	50, 146	120
5	50, 146	70

ries of inversions, indicating a good performance of the algorithm to reach regions of low misfit.

5.3. Systematic study

As mentioned above, inversion results are case dependent and different accuracies on the parameter estimates were obtained depending on the location, width and sound-speed profile of the middle cell. In addition to these environmental parameters, the positions of the source and array also affect the inversion results. Those are interesting parameters to study since they are under human control and relatively easy to vary. In the following, the effect of the depth of the hydrophones and the source depth (Z_s) are systematically investigated through different inversion scenarios (Table III).

In all scenarios, the parameters not defined in Table III were identical to those given in Table I. No transition cells were present when calculating the simulated pressure fields but correlated noise was added to the data such that the SNR was 10 dB at each hydrophone. This level of noise corresponds to a realistic experimental situation. For each scenario, three inversions were repeated for 10 time windows (the range-independent profile was not investigated), three middle-cell widths (2, 7, 12 km), and three middle-cell locations (5, 11, 17 km). In each inversion, a different realization of correlated noise was used.

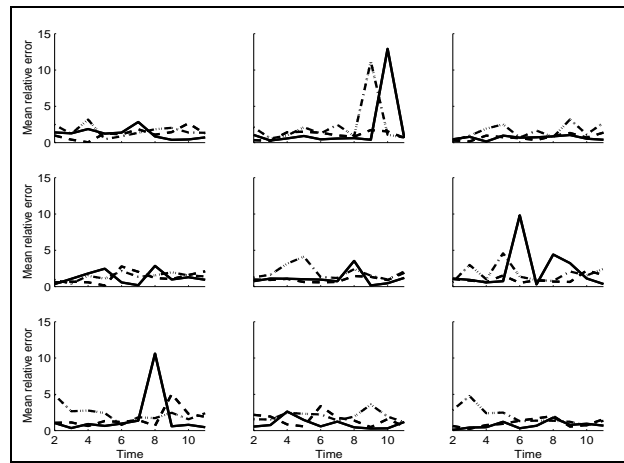


Figure 14. Variability of the parameter mean relative error (ϵ) with the vertical position of the array, the position of the middle cell and the width of the middle cell. From left to right the depth of the shallowest receiver of the two array sections were {50, 82}, {50, 146} and {114, 146} m (scenarios 3, 1, 2). From top to bottom, the middle cell was 5, 11 and 17 km from the source. The different lines indicate the width of the middle cell: solid line for 12 km, dashed line for 7 km and dash-dotted line for 2 km.

The parameter mean relative error corresponding to the minimum misfit encountered during the three inversions is shown in Figures 14 and 15 for the various scenarios. The error varies with the array and source positions (the effect of different noise realizations is considered negligible here) but no obvious trend can be seen. The receivers and source positions as well as the filament properties (location, width, sound speed) are parameters that all affect the inversion results. However there are no clear predominance of one of these parameters on the other.

In the few cases where the error is larger than 5 (cases concentrated in time windows 7-10), the inversion algorithm consistently failed to find a minimum misfit smaller than the misfit calculated with the true value. This poor performance can be due to a greater complexity of the parameter spaces to sample (see example in Figure 16).

On average, the error is two orders of magnitude larger than the error found in the ideal case (Figure 6). However, in most cases, the upwelling is still clearly visible as shown in Figure 17 which illustrates the sound-speed estimates for a non-optimal result (red line of left bottom panel of Figure 14). For this particular case, the average temperature absolute error over time and depth is 0.14°C .

6. Conclusion

In this paper, the performance of a MFI method based on a simplistic ocean model for upwelling filament detection and tracking was investigated. The problem consisted in estimating the sound-speed profile associated with the filament, its location and its width, as well as their variations in time. The challenge was to do so with a single pair of source-vertical array.

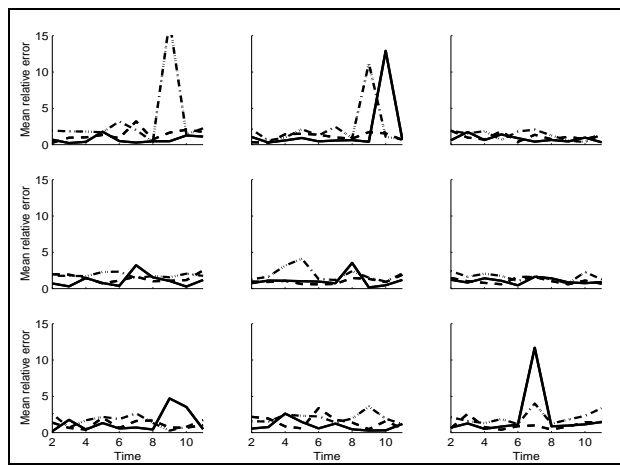


Figure 15. Variability of the parameter mean relative error (ε) with the source depth, the position of the middle cell and the width of the middle cell. From left to right the source depth was 120, 90 and 70 m (scenarios 4, 1, 5). From top to bottom, the middle cell was 5, 11 and 17 km from the source. The different lines indicate the width of the middle cell: solid line for 12 km, dashed line for 7 km and dash-dotted line for 2 km.

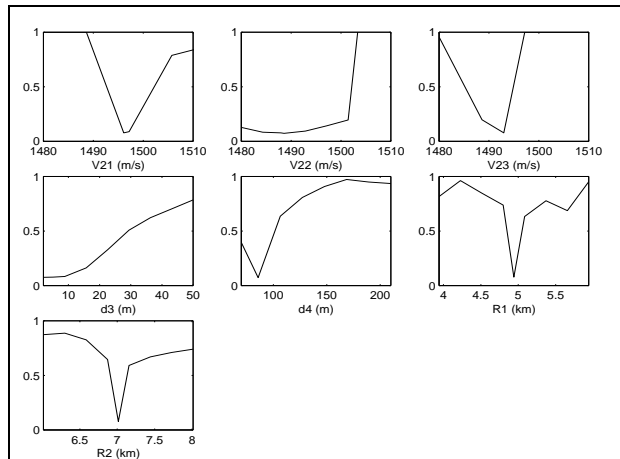


Figure 16. Variations of the misfit with individual parameter, the remaining parameters being fixed to their true value for scenario 4, time window 9, cell width 2 km, cell position 5 km from source. The line shows the average misfit obtained for 10 realizations of correlated noise for a 10 dB SNR.

Simulation studies showed that the parameter estimates were rapidly and well determined in the ideal case where no source of mismatch was present. The sound speed profile and the position of the filament relative to the array and source appeared to have the most effect on the inversion results. With correlated noise in the data, the estimates were still well estimated for a 10 dB SNR but significantly degraded at 5 dB. Nevertheless, at 5 dB, the global rise of cold water was well visible. Finally, the addition of transition cells in the true waveguide model increased the level of misfit. However, up to a transition-cell width of ($2 \times$) 500 m, the parameter estimates were relatively good and it was possible to detect and localize the filament.

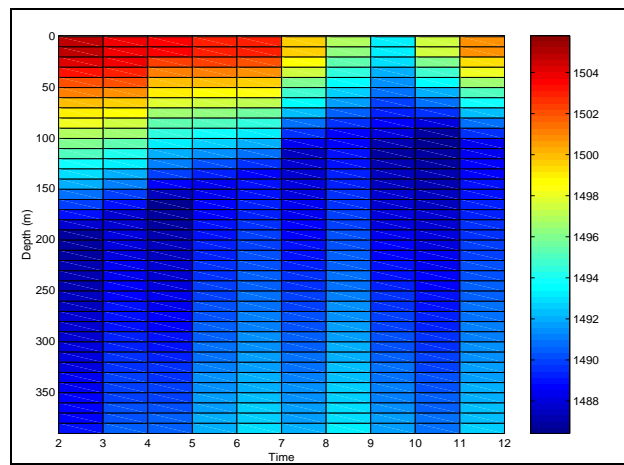


Figure 17. Estimated sound-speed profiles in the middle cell for scenario 3, cell width 7 km, distance from source 11 km. The true profiles are given in Figure 3.

A systematic study of the performance of the inversion for various properties of the filament and positions of the array and the source emphasized the dependence of the parameter estimates accuracy to all of these parameters but without clear predominance of any of them. On the other hand and despite the presence of noise, the upwelling could be clearly seen in most cases.

The results obtained in the above simulations showed the feasibility of monitoring an upwelling with a single pair of source-array, even in non-ideal conditions. In the future, other important sources of mismatch such as more complex sound-speed profiles or inaccurate knowledge of the hydrophone position should be studied before the experimental test.

Acknowledgement

This work was sponsored by the Fundação para a Ciência e a Tecnologia (Portugal), under contract PD-CTM/P/MAR/15296/1999. In addition, the careful and thorough efforts of the reviewers of this manuscript are thoughtfully appreciated

References

- [1] R. Haynes: Eulerian and lagrangian observations in the Iberian coastal transition zone. Ph.D. thesis, Univ. of Wales, Bangor, 1993.
- [2] P. Relvas: The physical oceanography of the Cape São Vicente upwelling region observed from sea, land and space. Ph.D. thesis, Univ. of Wales, Bangor, 1999.
- [3] W. Munk, P. Worcester, and C. Wunsch: Ocean acoustic tomography. Cambridge U. P., Cambridge, 1995.
- [4] A. Tolstoy, O. Diachok and L.N. Frazer: Acoustic tomography via matched field processing. *J. Acoust. Soc. Am.* **89** (1991) 1119–1127.
- [5] M.D. Collins and W.A. Kuperman: Focalization: Environmental focusing and source localization. *J. Acoust. Soc. Am.* **90** (1991) 1410–1421.

- [6] M. Gerstoft and D.F. Gingras: Parameter estimation using multifrequency range-dependent acoustic data in shallow water. *J. Acoust. Soc. Am.* **99** (1996) 2839–2850.
- [7] P.T. Strub, P.M. Kosro and A. Huyer: The nature of the cold filaments in the California Current System. *J. Geophys. Res.*, **96(C8)** (1991) 14743–14768.
- [8] R.K. Dewey, J.N. Moun, C.A. Paulson, D.R. Caldwell and S.D. Pierce: Structure and dynamics of a coastal filament. *J. Geophys. Res.*, **96(C8)** (1991) 14885–14907.
- [9] S.R. Ramp, P.F. Jessen, K.H. Brink, P.P. Niiler, F.L. Daggett and J.S. Best: The physical structure of cold filaments near Point Arena, California, during June 1986. *J. Geophys. Res.*, **96(C8)** (1991) 14859–148838.
- [10] K.H. Brink and T.J. Cowles: The coastal transition zone program. *J. Geophys. Res.* **96(C8)** (1991) 14637–14647.
- [11] R. Haynes, E.D. Barton and I. Pilling: Development, persistence and variability of upwelling filaments off the Atlantic coast of the Iberian Peninsula. *J. Geophys. Res.* **98(C12)** (1993) 22681–22692.
- [12] C.M. Ferla, M.B. Porter and F.B. Jensen: C-SNAP: Coupled SACLANTCEN normal mode propagation loss model. Memorandum SM-274, SACLANTCEN Undersea Research Center, La Spezia, Italy, 1993.
- [13] W.H. Press, B.P. Flannery, S.A. Teukolsky and W.T. Vetterling: *Numerical Recipes - The Art of Scientific Computing* 2nd ed.. Cambridge University Press, Cambridge, 1992.
- [14] D.E. Goldberg: *Genetic algorithms in search, optimization and machine learning* Addison Wesley Publishing company, Reading, MA, 1989.
- [15] M. Musil, M.J. Wilmut and N.R. Chapman: A hybrid simplex genetic algorithm for estimating geoacoustic parameters using matched-field inversion. *IEEE J. of Oceanic Engineering* **24** (1999) 258–269.
- [16] V. Corré and N. R. Chapman: Vertical-slice matched-field tomography. *Acta Acustica.* **87** (2001) 637–646.
- [17] A.N. Gavrilov and P.N. Mikhalevsky: Recent results of the ACOUS (Arctic Climate Observation using Underwater Sound) program. Proceedings of the Sixth European Conference on Underwater Acoustics, ECUA'2002 (2002) Gdansk, Poland.
- [18] C.S. Clay and H. Medwin: *Acoustical oceanography*. Wiley-Interscience, New York, 1977.